Wide-Range Adaptive IPT Using Dipole-Coils With a Reflector by Variable Switched Capacitance

Eun S. Lee, *Student Member, IEEE*, Byeong G. Choi, *Student Member, IEEE*, Jin S. Choi, *Student Member, IEEE*, Duy T. Nguyen, *Member, IEEE*, and Chun T. Rim, *Senior Member, IEEE*

***Abstract*—A dipole-coil-based inductive power transfer (IPT) with a reflector, which first adopts the variable switched capacitance for load power regulation under very wide-range distance variation between transmitter (Tx) and receiver (Rx) coils, is newly proposed. The resonant frequency of the LC tank of the proposed IPT can be appropriately modulated by the variable switched capacitance with reliable zero-voltage-switching (ZVS) operations. Therefore, even though the distance changes very widely, load power can be regulated solely by the variable switched capacitance in the Rx circuit without complicated communication links between the Tx and Rx coils. A detailed static analysis based on a recent imaginary gyrator model and design procedure for the proposed IPT are presented to build a simplified LC resonant tank of the proposed IPT and ZVS condition and to identify applicable distance variation range for constant load power. A prototype of the Tx and Rx coils for 100 W of load power, considering average power consumptions of home appliances, was fabricated and verified by simulations and experiments, which showed that load power was completely regulated to 100 W for 23–70 cm of very wide-range distance variation at a fixed switching frequency of 140 kHz.**

***Index Terms*—Dipole coil resonance system (DCRS), inductive power transfer (IPT), load power regulation, reflector, variable switched capacitance, wide-range distance variation between Tx and Rx coils, zero voltage switching (ZVS).**

I. Introduction

WIRELESS power transfer (WPT) has been widely used in many technologies such as electric vehicles, mobile devices, Internet of things, medical devices, and home appliances by virtue of providing electric power without cumbersome cables, creating clean and uncluttered-looking electronic devices and an inherent way to avoid electrical accidents. Contact- and non-contact-type of WPT systems with less than 5 cm distance between the transmitter (Tx) and receiver (Rx) are prominent in markets for mobile devices and home appliances. However, as customers require the freedom of using WPT, these conventional types of short-distance WPT are no longer a viable solution to fulfill the requirements of the customers. Thus, numerous WPT technologies have been introduced to transfer a high load power at long distance [1]–[28]. One such candidate, coupled magnetic resonance systems have been developed since their introduction in 2007 [1]–[7]. This system, however, adopts four large resonant coils and operates at several MHz for a very high quality factor (∼2,000); hence, the system has inherent demerits, which are large voltage stress of resonant capacitors in each coil, inherent bulky and volumetric structures, and hypersensitivity to the surrounding conditions such as temperature, humidity, and human proximity. Radio frequency (RF) and infrared (IR) types of WPT systems may be a solution due to their characteristic straightness from the Tx to the Rx [8]–[13]. However, the RF-type WPT has inherent EMF/EMI problems, low power efficiency, low power density (kW/m^3), and cannot penetrate metal objects [8]–[10]. The IR-type WPT is also incapable of penetrating obstacles, has low power efficiency and density, and requires very precise control to align the Tx and Rx through a straight beam [11]–[13]. On the other hand, inductive power transfer (IPT) systems are known to be suitable for long distance WPT applications; 209 W at 5 m and 11 W at 7 m of long distance wireless power delivery have been achieved by the dipole coil resonance system (DCRS) [14]–[15]. The DCRS adopts long slim-size dipole coils operating at a relatively low switching frequency (several tens of kHz) with a low quality factor (∼100), which is beneficial to adopt various practical applications with a simple structure and less sensitive characteristic. It was proven that a Tx reflector, which is a metal plate and placed behind the Tx coil, is effective to increase the power efficiency while delivering the same load power [23]. Therefore, IPT based on the DCRS with the Tx reflector is highly applicable to long distance WPT applications with high power transfer capability.

In spite of merits of IPT due to its low quality factor, load characteristics of IPT such as load voltage, load power, and power efficiency inevitably change when the distance d between Tx and Rx coils varies, i.e., the variation of the coupling factor k, as shown in Figs. 1 and 2. The tuning methods based on saturable reactors in a Class E inverter were adopted to regulate the load power under k changes [24]–[25]. However, the dc current of saturable reactors, switching frequency, and duty cycle should

Manuscript received June 21, 2016; revised August 16, 2016 and October 23, 2016; accepted November 26, 2016. Date of publication December 9, 2016; date of current version May 9, 2017. This work was supported by the National Research Foundation of Korea (NRF) grant funded by the Korea government (Ministry of Science, ICT & Future Planning) (NRF-2016R1A5A1013919). Recommended for publication by Associate Editor O. C. Onar.

E. S. Lee, B. G. Choi, and J. S. Choi are with the Department of Nuclear and Quantum Engineering, Korea Advanced Institute of Science and Technology, Daejeon 34141, South Korea (e-mail: eunsoo86@kaist.ac.kr; choibk09@kaist.ac.kr; chjs0327@kaist.ac.kr).

D. T. Nguyen is with MKS Korea Co. Ltd, Daejeon 34028, South Korea (e-mail: Duy_Nguyen@mksinst.com).

C. T. Rim is with GIST, Gwangju 61005, South Korea (e-mail: ctrim@gist.ac.kr).

Color versions of one or more of the figures in this paper are available online at http://ieeexplore.ieee.org.

Digital Object Identifier 10.1109/TPEL.2016.2637931

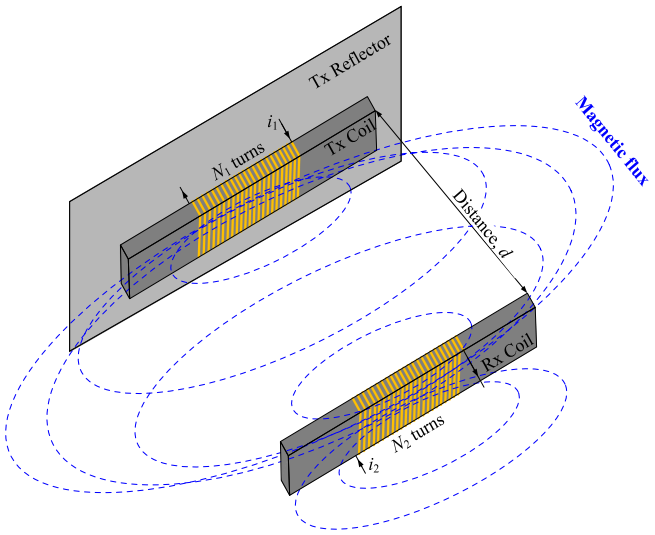

Fig. 1. Overall Tx and Rx coil configuration of the proposed IPT with the Tx reflector.

be precisely controlled not only to regulate load power but also to guarantee zero voltage switching (ZVS) and zero-voltage derivative switching operations of the Class E inverter. In addition, due to high sensitive characteristics of load resistance and distance variations for reliable operation of the Class E inverter, it may not be suitable for practical applications. Additional circuits such as dc–dc converters in Tx and Rx coils, isolation-type feedback control circuits between Tx and Rx coils, and wireless communication links are required to regulate load power, which increases cost and complexity of the whole WPT system [26]–[28].

In this paper, an adaptively controlled variable switched capacitance is first applied to a dipole-coil-based loosely-coupled IPT system with a Tx reflector, which can regulate load power under very wide-range distance variation, as shown in Fig. 3. The equivalent circuit of the proposed IPT can be represented as an LC parallel resonant circuit, as shown in Fig. 5. The equivalent capacitance of the variable switched capacitance can be appropriately modulated, which controls the resonant frequency of the LC tank in the Rx circuit and finally regulates load power. Contrary to the conventional variable switched capacitance circuits [35]–[38], the proposed IPT simply uses two main switches S_1 and S_2 in the Rx rectifier circuit for adaptive control of the variable switched capacitance and one comparator with sensing resistors for ZVS operations of S_1 and S_2; hence, the proposed IPT is applicable to the home appliances due to its simple structure and the low cost of the whole system. The validity of the proposed IPT is verified by simulations and experiments, showing a complete load power regulation over the wide-range distance variation.

II. Theoretical Consideration of the Variable Switched Capacitance

It is important to modulate the switching frequency or resonant frequency of the LC tank so that the load characteristics are appropriately controlled. Switching frequency can be modulated to control the load power when the other parameters are fixed [29]–[31]. However, it may not be easy to satisfy the design goals with the ZVS operation of Tx inverter due to two fixed resonant frequencies of the Tx and Rx coils, which require complicated algorithms and control circuits. In particular, the cumbersome communication links between the Tx and Rx are essential to sense the load voltage and to give Tx control circuit. One of the methods to modulate the resonant frequency of the LC tank is to simply add or remove the capacitors, which are electrically connected or disconnected by the switches, the microcontroller unit (MCU), and additional control circuits [32]–[34]. However, this method has no precise control capability due to its quantized values of each capacitor. Although binary weighted capacitors controlled by MCU may be adopted to control the specific capacitance, it requires a number of additional capacitors and complicated control circuits [34]. On the other hand, the variable switched capacitance becomes a promising solution to modulate the equivalent capacitance and has been widely applied to WPT applications due to its compact size with the high voltage rating of the capacitors, desirable soft-switching operation of main switches, easy applicability to high switching frequency operation [35]–[38]. This variable switched capacitance can be modulated by the switching duty cycle of controlled main switches *D*, which results in adaptive change of equivalent capacitance by considering the fundamental components of the voltages and currents, as shown in Fig. 4, where v_c is the voltage in the parallel capacitor C_p in Fig. 3, v_{c1} is the fundamental components of v_c, and v_L is the load voltage. Recently, the variable switched capacitance was first applied to LED drivers, which adopt bidirectional switching circuits with ZVS operations of main switches compatible with wide range of switching frequencies [38]. In Fig. 4, equivalent capacitance of the variable switched capacitance with bidirectional switches was theoretically derived by switching duty cycle *D* determined by v_{gs1} and v_{gs2} as follows [38]:

$$C_v \equiv \frac{C_p}{1-2D-\frac{1}{\pi}\sin 2\pi D} \text{ for } 0 \le D < 0.5. \qquad (1)$$

As shown in Fig. 4, the switching waveform of v_c is determined by C_p, assuming the other parameters such as C_L, R_L, and f_s are fixed. From (1), equivalent capacitance C_v by switching duty cycle *D* is derived when the load effect of the diode rectifier is neglected and v_c is a complete sinusoidal waveform, which corresponds to Fig. 4(c); the peak voltage of v_c is always less than V_L, and the diode rectifier operates in discontinuous conduction mode (DCM) [42]–[46]. Contrary to this, the diode rectifier almost operates in continuous conduction mode (CCM) if a very small value of C_p is used, as shown in Fig. 4(a). The peak voltage of v_c is abruptly clamped to V_L, and the waveform of v_c is nearly rectangular; the equivalent capacitance of Fig. 4(a) no longer matches the theoretical analysis of (1) due to the nonsinusoidal waveform of v_c. In this case, the conversion ratio of α, which is the ratio of V_c and V_L considering the fundamental components, is nearly 0.9 [42]–[46]. Because the general switching waveform of v_c has finite charging times of t_{c1} and t_{c2}, as shown in Fig. 4(b), α depends on t_{c1} and t_{c2} as

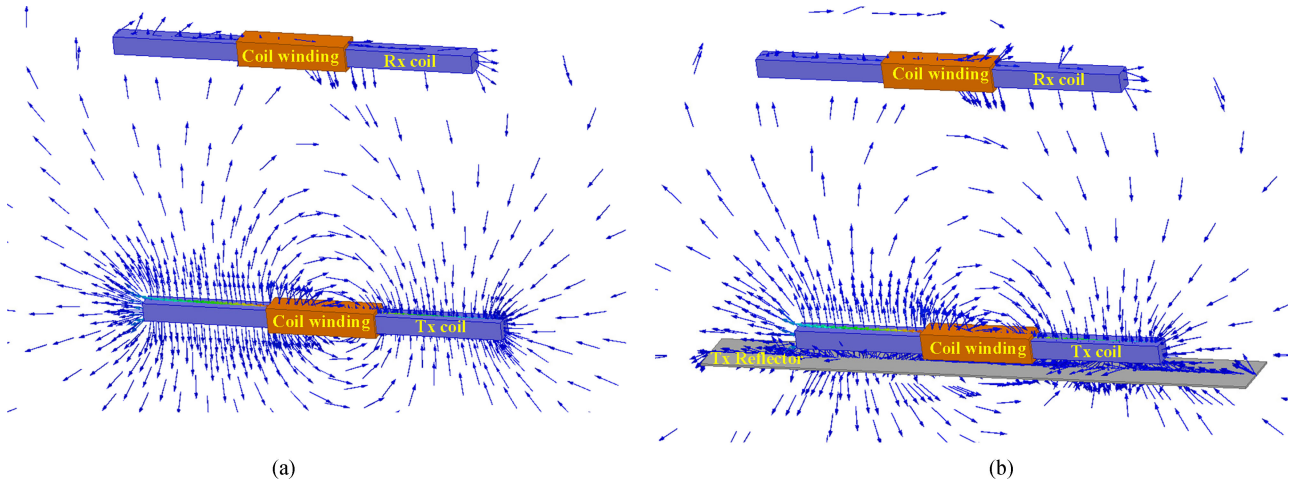

Fig. 2. Simulation results of the magnetic flux vector lines for the proposed IPT performed by 3-D Maxwell simulations, where $d = 70$ cm, $I_1 = 10$ A, and $I_2 = 0$. (a) Without a Tx reflector. (b) With a Tx reflector.

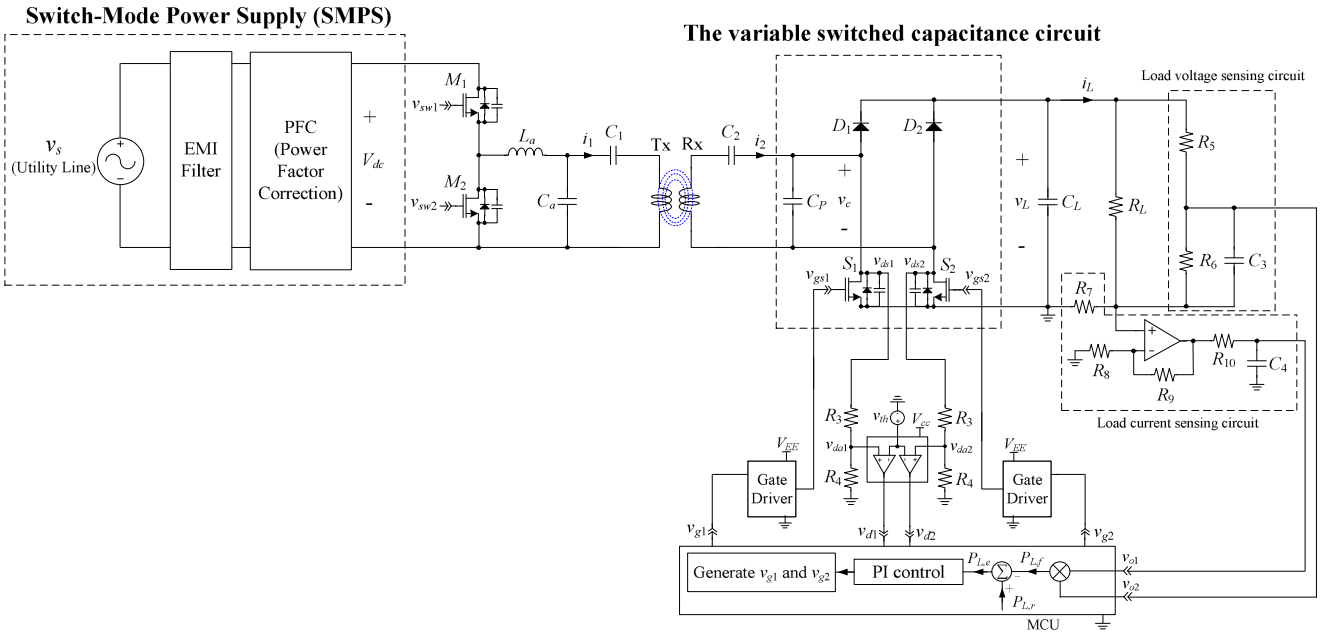

Fig. 3. Overall circuit diagram of the proposed IPT with the switch-mode power supply and the variable switched capacitance.

follows [46]:

$$V_c = \alpha(t_{c1}, t_{c2})V_L, R_e = \alpha^2(t_{c1}, t_{c2})R_L \tag{2}$$

where R_e is equivalent resistance seen from the diode rectifier.

From (2), it is extremely complicated to find the expression for this highly nonlinear α, which is the functions of t_{c1} and t_{c2} according to analysis; therefore, such an expression can be found only by comparing the experimental results w.r.t. the different cases of C_p, which will be discussed in detail in Section VI.

III. Static Analysis of the Proposed IPT

The proposed IPT, as shown in Figs. 1 and 2, is based on conventional slim-size dipole Tx and Rx coils [14]–[15] so that static performance of the variable switched capacitance for load power regulation is verified. For long distance IPT systems, several Tx and Rx coil structures can be a candidate to be adopted [1]–[22]. Long slim-size dipole coil structures are more preferred than the other coil structures for home appliance applications because dipole coil structures are shaped as line having very small width, which are neither plane nor volumetric structures. Thus, dipole coil structures will be recommended to the home appliances in terms of easily installation under confined spaces. The magnetic field distributions of the proposed IPT for with and without a Tx reflector cases are described in Fig. 2, representing that magnetic flux generated by Tx coil is effectively interlinked to Rx coil. Regarding effect of a reflector, it is not possible to analytically build an explicit modeling of a reflector by quantitative values. Instead, it has been experimentally identified that a Tx reflector adopted behind Tx

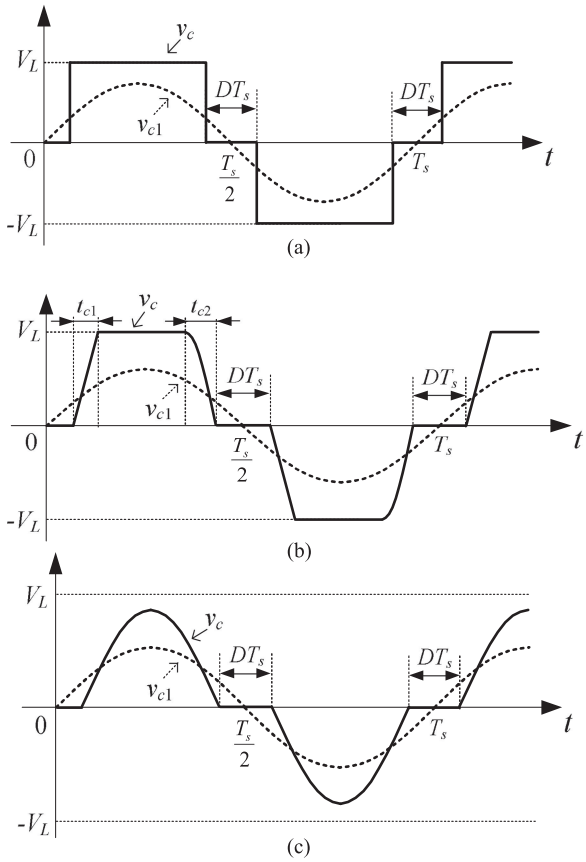

Fig. 4. Switching waveforms of v_c, depending on the parallel capacitance C_p. (a) Very small C_p (t_{c1} and $t_{c2} \approx 0$), (b) Reasonable C_p, (c) Very large C_p.

coil enhances the power efficiency for long distance IPT based on DCRS [23]. As shown in Fig. 2(b), self-inductance of the Tx coil L_1 decreases due to the reduction of leakage magnetic flux behind the Tx coil, i.e., the leakage magnetic flux inside the Tx coil reduces, which is beneficial to reduce core loss of the Tx coil and finally to enhance the power efficiency [23]. As shown in Fig. 3, the switch-mode power supply, which is typically composed of an EMI filter and a power factor correction (PFC), is generally used; hence, an EMI issue caused by high frequency switching operation is no concern, and electric devices connecting to the utility line operate with high power factor (PF) and low total harmonic distortion (THD) to satisfy the international standards [47]–[48]. Input voltage of the asymmetric half-bridge inverter in Fig. 3 is constant dc voltage V_{dc}, and L_a and C_a are adopted to generate a constant source current. Primary-series-secondary-series resonant capacitors C_1 and C_2 are adopted as an example in this paper to nullify the reactance of the Tx and Rx coils, respectively. The other resonant topologies, such as primary-series-secondary-parallel for both voltage and current sources, can be also adopted for the variable switched capacitance, though not shown in this paper [50]. The variable switched capacitance circuit is composed of two main switches S_1 and S_2 and two fast recovery diodes D_1 and D_2 with a lumped parallel capacitor C_p. Circuit topology of the variable switched capacitance circuit is similar with active rectifiers [39]–[41]. However, contrary to those conventional active rectifiers [39]–[41], secondary rectifier of the proposed IPT adopts C_p with an active rectifier circuit so that C_p is utilized as the variable switched capacitance; hence, the proposed variable switched capacitance circuit requires a small number of components compared to conventional one adopted to versatile LED drivers [38]. Nevertheless, the functionality of the variable switched capacitance is identical to the conventional one, which will be identified in Section IV. To ensure the ZVS operations of S_1 and S_2, the comparator with sensing resistors is adopted to sense the v_{ds1} and v_{ds2}, and to feed v_{d1} and v_{d2} to the MCU. The load voltage v_L and the load current i_L are sensed by the load voltage and current sensing circuits, and the load capacitor C_L is connected to the output of the rectifier for smoothing v_L.

A. Load Power P_L

The proposed IPT in Fig. 3 can be represented in Fig. 5 by an imaginary gyrator-based circuit modeling, which is a simple and systematic ways to analyze the IPT with graphical procedures [49]. In Fig. 5, *M* is mutual inductance, and r_1 and r_2 include the equivalent series resistances (ESRs) of capacitors C_1 and C_2 and core and copper losses of the Tx and Rx coils, respectively. Especially, effect of the Tx reflector causes decrement of L_1 and increment of r_1, whose variations are adopted throughout this paper [23]. The variable switched capacitance circuit is regarded as C_v and load resistance R_L can be represented as equivalent resistance R_e, as identified from (1) and (2). Assuming that only fundamental components of the voltages and currents are considered and the switching duty cycle of the inverter is 0.5, the output voltage of the asymmetric half-bridge inverter V_1 is determined as follows [42]–[46]:

$$V_1 = \frac{2\sqrt{2}}{\pi} \cdot \frac{V_{dc}}{2} \approx 0.45\, V_{\rm dc}. \tag{3}$$

By applying Thevenin's theorem to the left part of the circuit of Fig. 5, an equivalent Thevenin circuit is obtained, as shown in Fig. 6(a), where it is assumed that L_1 and C_1, and L_2 and C_2 are fully resonated, respectively. Then, the Thevenin voltage source $V_{\rm a}$ is derived as follows:

$$V_a = \frac{V_1}{X_a} \tag{4a}$$

$$\because X_a \equiv 1 - \omega_s^2 L_a C_a,\ f_a \equiv \frac{1}{2\pi\sqrt{L_a C_a}} \tag{4b}$$

$$f_s = f_{r1} = f_{r2} \left(\because f_{r1} \equiv \frac{1}{2\pi\sqrt{L_1 C_1}}, f_{r2} \equiv \frac{1}{2\pi\sqrt{L_2 C_2}} \right) \tag{4c}$$

where f_s and f_a are the switching frequency of the inverter and the resonant frequency of L_a and C_a, respectively.

According to the gyrator characteristics, the Thevenin voltage source and impedance in Fig. 6(a) can be transformed to the current source I_g with equivalent inductance L_e and resistor r_{g1}

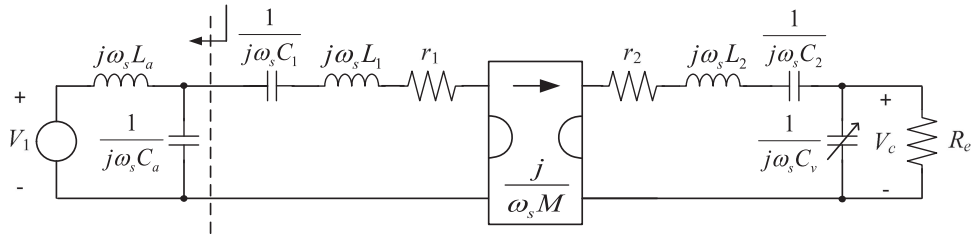

Fig. 5. Simplified equivalent circuit of Fig. 3 with a gyrator, substituting the proposed variable switched capacitance circuit as C_v.

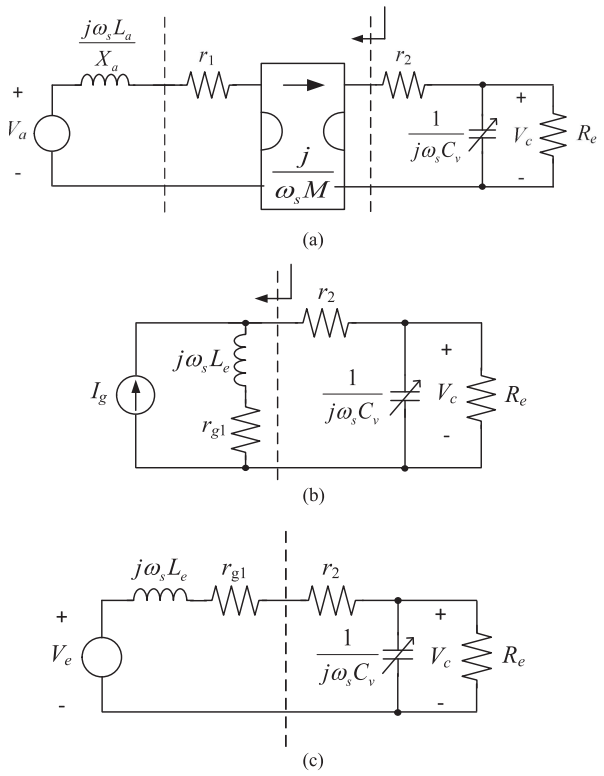

Fig. 6. Simplified final static circuit of the proposed IPT from the load-side viewpoint. (a) Equivalent Thevenin circuit of Fig. 5, assuming that L_1&C_1 and L_2&C_2 are fully resonated. (b) Equivalent circuit of (a), eliminating a gyrator. (c) Simplified final static circuit of (b).

Fig. 6(b) as follows [49]:

$$I_g = \frac{jV_a}{X_m} = \frac{jV_1}{X_m X_a} \tag{5a}$$

$$L_e = \frac{-L_a X_m^2 X_a}{r_1^2 X_a^2 + \omega_s^2 L_a^2} > 0 \ (\because X_a < 0), r_{g1} = \frac{r_1 X_m^2 X_a^2}{r_1^2 X_a^2 + \omega_s^2 L_a^2} \tag{5b}$$

$$\because X_m \equiv \omega_s M. \tag{5c}$$

As shown in Fig. 6(c), the simplified final equivalent circuit, which is an LCR parallel resonant circuit, can be obtained, where equivalent source voltage V_e is as follows:

$$V_e = I_g \cdot (j\omega_s L_e + r_{g1}) = \frac{jX_m V_1}{r_1 X_a + j\omega_s L_a}. \tag{6}$$

As identified from (4b) and (5b), the equivalent inductance L_e should be positive, i.e., $X_a < 0$ ($\because f_s > f_a$), in this paper so that L_e is regarded as an inductance and the final equivalent circuit is composed of an LCR parallel resonant circuit in Fig. 6(c).

From (5) and (6), the voltage gain G_V and load power P_L are finally determined as follows: (7) shown at the bottom of this page.

B. Source Power P_S and Efficiency η

The source power P_s for power efficiency can be calculated from Fig. 7, which shows the equivalent circuit from the source-side viewpoint. By applying the Norton equivalent theorem of Fig. 5 and converting the parallel connection of R_e and C_v in Fig. 5 to the series connection, Fig. 5 can be converted to Fig. 7(a), where I_s, C_v' and R_e' are derived, as follows:

$$I_s = \frac{V_1}{j\omega_s L_a} \tag{8a}$$

$$R_e' = \frac{R_e}{1 + \omega_s^2 C_v^2 R_e^2}, C_v' = \frac{1 + \omega_s^2 C_v^2 R_e^2}{\omega_s^2 C_v R_e^2}. \tag{8b}$$

Similar to Fig. 6(b), by eliminating the gyrator in Fig. 7(a), the simplified final static circuit from the source-side viewpoint can be obtained, as shown in Fig. 7(b), where L_g and r_{g2} are defined, as follows:

$$L_g = \frac{C_v' X_m^2}{1 + \omega_s^2 C_v'^2 (r_2 + R_e')^2}, \ r_{g2} = \frac{\omega_s^2 C_v'^2 X_m^2 (r_2 + R_e')}{1 + \omega_s^2 C_v'^2 (r_2 + R_e')^2}. \tag{9}$$

$$\therefore G_V \equiv \left|\frac{V_c}{V_e}\right| = \frac{R_e}{\sqrt{\{R_e (1 - \omega_s^2 L_e C_v) + r_{g1} + r_2\}^2 + \omega_s^2 \{L_e + C_v R_e (r_{g1} + r_2)\}^2}} \tag{7a}$$

$$P_L \equiv \frac{V_L^2}{R_L} = \frac{|V_c|^2}{R_e} = \frac{R_e |V_e|^2}{\{R_e (1 - \omega_s^2 L_e C_v) + r_{g1} + r_2\}^2 + \omega_s^2 \{L_e + C_v R_e (r_{g1} + r_2)\}^2}. \tag{7b}$$

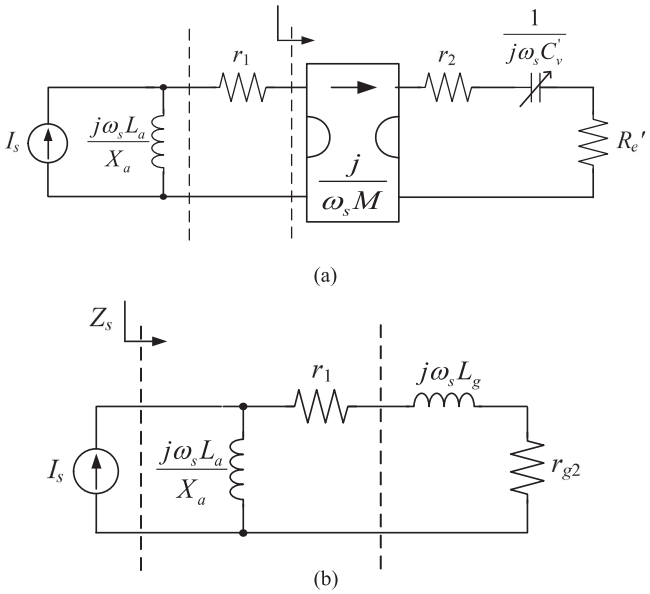

Fig. 7. Simplified final static circuit of the proposed IPT from the source-side viewpoint. (a) Equivalent Norton circuit of Fig. 5. (b) Simplified final static circuit of (a).

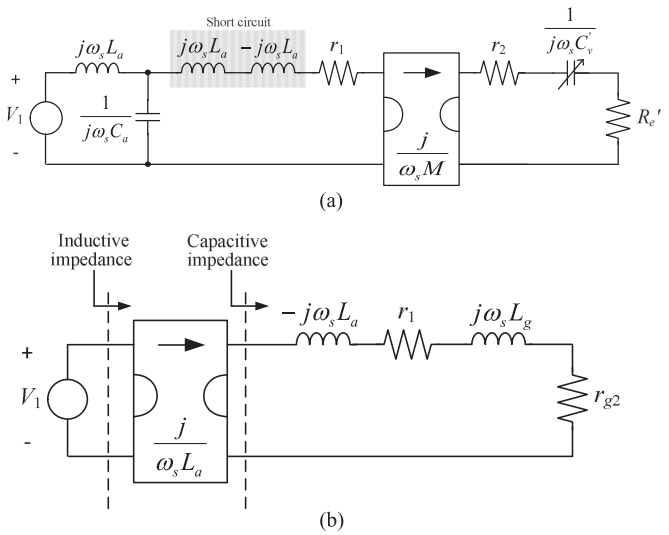

Fig. 8. Simplified static circuit of the proposed IPT from the source-side viewpoint for ZVS conditions of M_1 and M_2. (a) Equivalent circuit of Fig. 5 by inserting pure imaginary impedances. (b) Simplified static circuit of (a) with ZVS conditions of M_1 and M_2.

Finally, the source power P_s and the power efficiency η can be determined from (8) and (9) as follows:

$$\therefore P_s = |I_s|^2 \mathrm{Re}\{Z_s\} = \frac{(r_1 + r_{g2})\, V_1^2}{\omega_s^2 (L_a + X_a L_g)^2 + X_a^2 (r_1 + r_{g2})^2} \tag{10a}$$

$$\eta = \frac{P_L}{P_s} \tag{10b}$$

$$\because Z_s \equiv \frac{j\omega_s L_a}{X_a} // (j\omega_s L_g + r_1 + r_{g2}) = \frac{j\omega_s L_a (r_1 + r_{g2}) - \omega_s^2 L_a L_g}{j\omega_s (L_a + X_a L_g)^2 + X_a (r_1 + r_{g2})}. \tag{10c}$$

C. ZVS Conditions for M_1 and M_2

Although the distance is widely changed, ZVS conditions of M_1 and M_2 in the half-bridge inverter in Fig. 3 should be guaranteed. Assuming that L_1 and C_1, and L_2 and C_2 in Fig. 5 are fully resonated, respectively, and the parallel connection of R_e and C_v in Fig. 5 is converted to the series connection, then equivalent circuit can be obtained, as shown in Fig. 8(a). Pure imaginary impedances $j\omega_s L_a$ and $-j\omega_s L_a$, which are simply short circuit, are inserted to make another gyrator model [49]. By eliminating a gyrator having $j/(\omega_s M)$ of forward gain and inserting another gyrator model having $1/(j\omega_s L_a)$ of forward gain, the simplified static circuit from the source-side viewpoint can be obtained, as shown in Fig. 8(b), where the other circuit transformation process is similar with Fig. 7. Note that capacitive impedance of the gyrator output implies inductive impedance of the gyrator input [49]; hence, the gyrator output impedance should be capacitive, as shown in Fig. 8(b), so that the gyrator input impedance, which corresponds to output of the half-bridge inverter, is inductive, as follows:

$$-j\omega_s L_a + j\omega_s L_g < 0 \quad \rightarrow \quad \therefore L_a > L_g. \tag{11}$$

In (11), L_g can be calculated from (9), whose value depends on the distance d and switching duty cycle D. Therefore, L_g should be always lower than L_a under load power regulation to satisfy (11), which will be experimentally verified in Section V.

IV. Design of the Proposed IPT and Control Circuit

A. Design of the Proposed IPT

Throughout this paper, it is assumed that target of load power is set to be 100 W and distance variation range of wireless power delivery is 20–70 cm, considering average power consumptions of home appliances such as television, computer desktops, monitors, and electric rice cookers and typical distance range between home appliances and floor at home. To deliver 100 W of load power at the 70 cm-off maximum distance condition ($d = d_{\max}$), two slim-sized dipole coils are established for Tx and Rx with the Tx reflector, as shown in Fig. 1. The final goal of the proposed design procedure is to regulate the load power when d severely changes: at least 20–70 cm of distance variation should be managed, considering to account for various types of home appliance WPT, which is the design goal of this paper. Under the given Tx and Rx coil structures, L_1, L_2, and M in Fig. 5 were experimentally measured when d decreases from 70 to 20 cm, as listed in Table I, where L_1 includes the effect of the Tx reflector in Figs. 1 and 2. The self-inductance of L_1 and L_2 are slightly increased when d decreases, whose variation is not so large due to the loosely coupled IPT of the Tx and Rx cores. The physical dimensions and the other parameter selections of the Tx and Rx coils will be discussed in detail in Section V. Throughout this paper, it is assumed that

TABLE I
MEASURED AND CALCULATED PARAMETERS FOR 100 W PROTOTYPE IPT

d (cm)	L_1 (μH)	L_2 (mH)	M (μH)	k	L_e (μH)	r_{g1} (Ω)
70	823	2.270	42	0.031	40	7
60	823	2.271	54	0.039	66	12
50	823	2.273	79	0.058	142	27
40	824	2.275	111	0.081	278	53
30	825	2.279	149	0.108	500	95
20	840	2.312	227	0.163	1,170	222

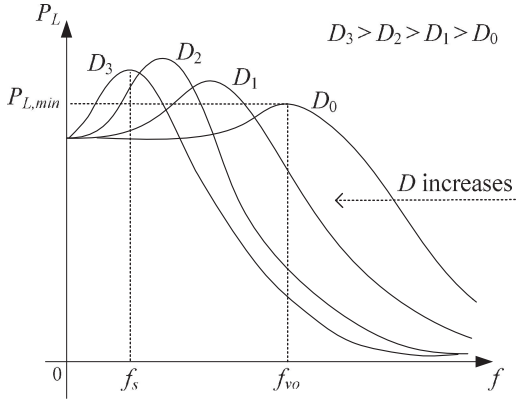

Fig. 9. Characteristic of P_L w.r.t. frequency f for various duties at $d = d_{\max}$.

the output voltage of the SMPS $V_{\rm dc}$, which corresponds to the output voltage of PFC in Fig. 3, is generally 400 V if the utility line voltage is 220 V/60 Hz and the PFC adopts the boost-type converter. The switching frequency is fixed to 140 kHz, considering the international standards of Wireless Power Consortium (WPC), AirFuel Alliance, and EN62233. Instead, the resonant frequency of LC tank $f_{\rm v}$ composed of L_e and C_v in Fig. 6(c) is modulated by switching duty cycle D as follows:

$$f_v(D) \equiv \frac{1}{2\pi\sqrt{L_e C_v(D)}}. \tag{12}$$

Therefore, the proposed design focuses on determining the remaining four parameters (L_a, C_a, C_p, and R_L) for regulating constant nominal load power $P_{L,\rm nom}$ with wide-range distance variation ($d_{\min} \le d \le d_{\max}$).

To find the appropriate values of those four parameters, the design procedure of the proposed IPT was established to satisfy the three assumptions shown below.

1) At $d = d_{\max}$, the initial resonant frequency f_{v0} when the duty is zero ($D = D_0$) should be larger than the switching frequency f_s at $D = D_0$, as shown in Fig. 9, i.e.,

$$f_{v0} > f_s \quad (\because f_{v0} = \frac{1}{2\pi\sqrt{L_e C_v(D_0)}}\ ,\ C_v(D_0) = C_p). \tag{13}$$

2) At $d = d_{\max}$, because the load power P_L is just below a nominal load power $P_{L,\rm nom}$, i.e., $P_L = P_{L,\min}$ at $D_0 = 0$ in Fig. 9, the operating point to satisfy $P_L \ge P_{L,\rm nom}$ should be reached by modulating $C_v(D)$. In other words, $f_{\rm v}$ decreases as D increases, and finally f_v will be equal to f_s under the condition that f_s is fixed at $D = D_3$, as shown in Fig. 9. To satisfy this condition, the maximum voltage gain $G_{V,\max}$, which can be derived from (7a) under $f_s = f_v$, should be at least larger than 1 as follows:

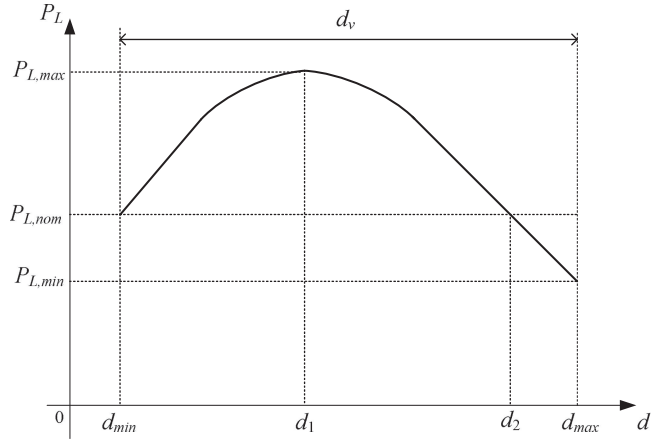

Fig. 10. Characteristic of P_L w.r.t. distance d without control of the variable switched capacitance.

$$G_{V,\max}|_{d=d_{\max}} = \frac{R_e}{\sqrt{\{Z_v(D) + R_e(r_{g1}+r_2)/Z_v(D)\}^2 + (r_{g1}+r_2)^2}} > 1 \quad (\because f_s = f_v) \tag{14a}$$

$$\because Z_v \equiv \sqrt{\frac{L_e}{C_v}}. \tag{14b}$$

As identified from (14), the maximum point of load power for each switching duty case when $f_s = f_v$, which corresponds to the maximum load voltage in (14a), decreases after it increases when the switching duty cycle starts to decrease from D_0, as shown in Fig. 9.

3) When d reaches the minimum required distance $d_{\min}$, P_L should be larger than or equal to $P_{L,\rm nom}$ for $D = 0$.

As pointed out in the above assumptions, the load power P_L will vary when the distance d changes from $d_{\max}$ to $d_{\min}$ without the variable switched capacitance, as shown in Fig. 10, where d_v is applicable distance variation range for constant load power regulation. By the proposed adaptive switching duty modulation to control the variable switched capacitance, the load power can be regulated, i.e., operating points to satisfy $P_L = P_{L,\rm nom}$ within $d_{\min} \le d \le d_{\max}$ always exist, as shown in Fig. 11.

To design the baseline of 100 W nominal load power delivery for 20 cm ($= d_{\min}$) $\le d \le$ 70 cm ($= d_{\max}$) throughout this paper, there are many possible combinations for the selection of those four circuit parameters (L_a, C_a, C_p, and R_L) based on the design goals with the above assumptions. In other words, it is not possible to analytically determine only one solution of L_a, C_a, C_p, and R_L. Accordingly, one of the possible combinations can be appropriately determined by numerical calculations; $L_a = 70.0\,\mu$H, $C_a = 36.2\,nF$, $C_p = 1.0\,nF$, and $R_L = 200\,\Omega$ were selected as an example, which is the small

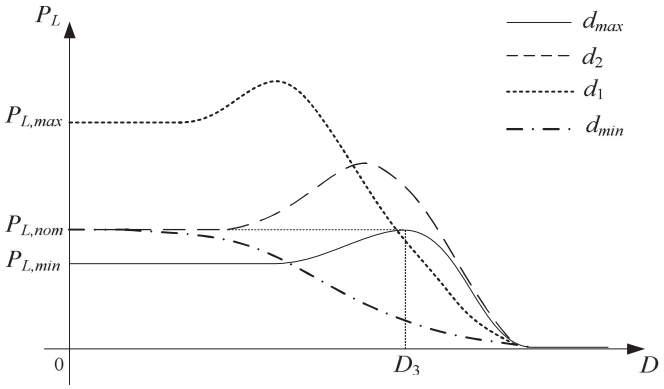

Fig. 11. Characteristic of P_L w.r.t. duty D for various distances by the proposed design procedure.

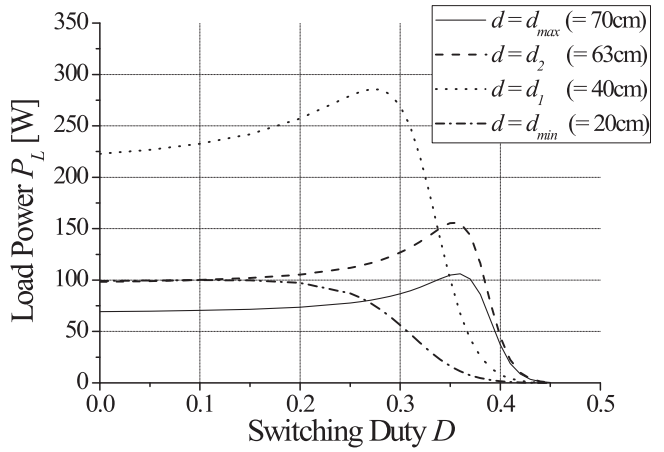

Fig. 12. Calculation results of P_L w.r.t. duty D for various distances at $f_s = 140$ kHz.

C_p case, as identified from Fig. 4(a). $f_a = 100$ kHz was selected, which satisfies (5b) to make equivalent inductance L_e at $f_s = 140$ kHz in Fig. 6(c).

Based on those parameters from the proposed design procedure, the load power was calculated from (7) w.r.t. the switching duty cycle D and switching frequency f_s, as shown in Figs. 12 and 13, where $d_{\max} = 70$ cm, $d_2 = 63$ cm, $d_1 = 40$ cm, and $d_{\min} = 20$ cm were found by calculation results. The conversion ratio α in (2) is selected as 0.75, whose selection will be discussed in detail in Section VI. The other parameters w.r.t. the distance d by the proposed static analysis are summarized in Table I. In Figs. 12 and 13(a), the load power is over 100 W of the nominal load power at $D = 0.35$ for $d = 70$ cm, and $D = 0$ for $d = 20$ cm, as identified from Figs. 10 and 11. f_v moves from f_{v0} to f_s in Fig. 9 as D increases and load power becomes maximum value when $f_v = f_s = 140$ kHz, i.e., $D = 0.35$, as shown in Fig. 13(a). For $d < 20$ cm, there is no satisfaction point for $P_L = 100$ W by modulating D in Fig. 12, i.e., $d < 20$ cm would not be covered for load power regulation. Nevertheless, applicable distance variation range of $d_v = 50$ cm in this paper may be enough by this extremely loosely coupled IPT for home appliance applications. Therefore, it is found that the variable switched capacitance can be appropriately modulated by controlling D so that load power is regulated for $d_v = 50$ cm, according to the proposed design procedure.

B. Operating Principle of the Proposed Control Circuit

To implement the functionality of the variable switched capacitance, it is important to achieve the soft switching operations of S_1 and S_2 for a reliable operation and high power efficiency of the proposed IPT. The proposed control circuit senses the drain-source voltages of both S_1 and S_2 and feeds the gate signals v_{gs1} and v_{gs2}; the signal and sensing grounds are the same, and cumbersome isolation circuits such as optocoupler are not necessarily used in the proposed IPT. Simply by voltage dividers composed of R_3 and R_4, as shown in Fig. 3, the drain-source voltages of S_1 and S_2 can be sensed as $v_{\rm da1}$ and $v_{\rm da2}$, respectively, and compared to threshold voltage $v_{\rm th}$, as shown in Fig. 14. Then, the rising edges of v_{d1} and v_{d2} are detected by MCU, and appropriate gate signals v_{gs1} and v_{gs2} are finally applied to main switches S_1 and S_2 through the gate drivers.

The detailed operating principle of the proposed control circuit for ZVS operation will be described in the following operating mode analysis, which includes four modes, as shown in Figs. 14 and 15. It is assumed that the equivalent resistances r_{g1} and r_2 in Fig. 6(c), the drain-source capacitances of two switches S_1 and S_2, the voltage drop of the all diodes, and the ESRs of all capacitors are neglected in this section for simplicity of analysis. The main switches S_1 and S_2 are the positive and negative polarity operations, respectively. The equivalent voltage v_e in Fig. 6(c) is represented as a sinusoidal waveform instead of including all of the parameter components for easily explanation. The operating modes begin when the secondary current i_2 $(= i_{\rm cp} + i_c)$ is just increased.

Mode 1 [t_0, t_1]: At t_0, the main switches S_1 and S_2 are turned OFF, as shown in Fig. 15(a). Nevertheless, the gate signal v_{gs1} was already applied even before the zero-crossing point that changes from negative to positive polarities of v_c for ZVS operation of S_1. Because v_c was negatively charged to $-V_L$ in the previous mode, it goes to zero through the positive current of $i_{\rm cp}$, as follows:

$$v_c(t) = -V_L \cos\omega_v(t - t_0) \text{ for } t_0 < t < t_1 \tag{15a}$$

$$i_{\rm cp}(t) = i_2(t) = \frac{V_E \sin\omega_s t_0 + V_L}{\omega_1 L_e} \times \sin\omega_v(t - t_0) \text{ for } t_0 < t < t_1 \tag{15b}$$

$$\because\ \omega_v \equiv \frac{1}{\sqrt{L_e C_p}},\ v_e = V_E \sin\omega_s t \tag{15c}$$

This mode ends when $v_{\rm c}$ changes from $-V_L$ to 0, and the time interval t_{10} is determined as follows:

$$t_{10} \cong \frac{\pi}{2\omega_v}. \tag{16}$$

Mode 2 [t_1, t_2]: At t_1, the switch S_1 and the body diode of switch S_2 are just turned ON, as shown in Fig. 15(b). In this case, because v_{ds1} was previously zero at the polarity transition point of $t = t_1$ and v_{gs1} was already applied, the ZVS operation of S_1

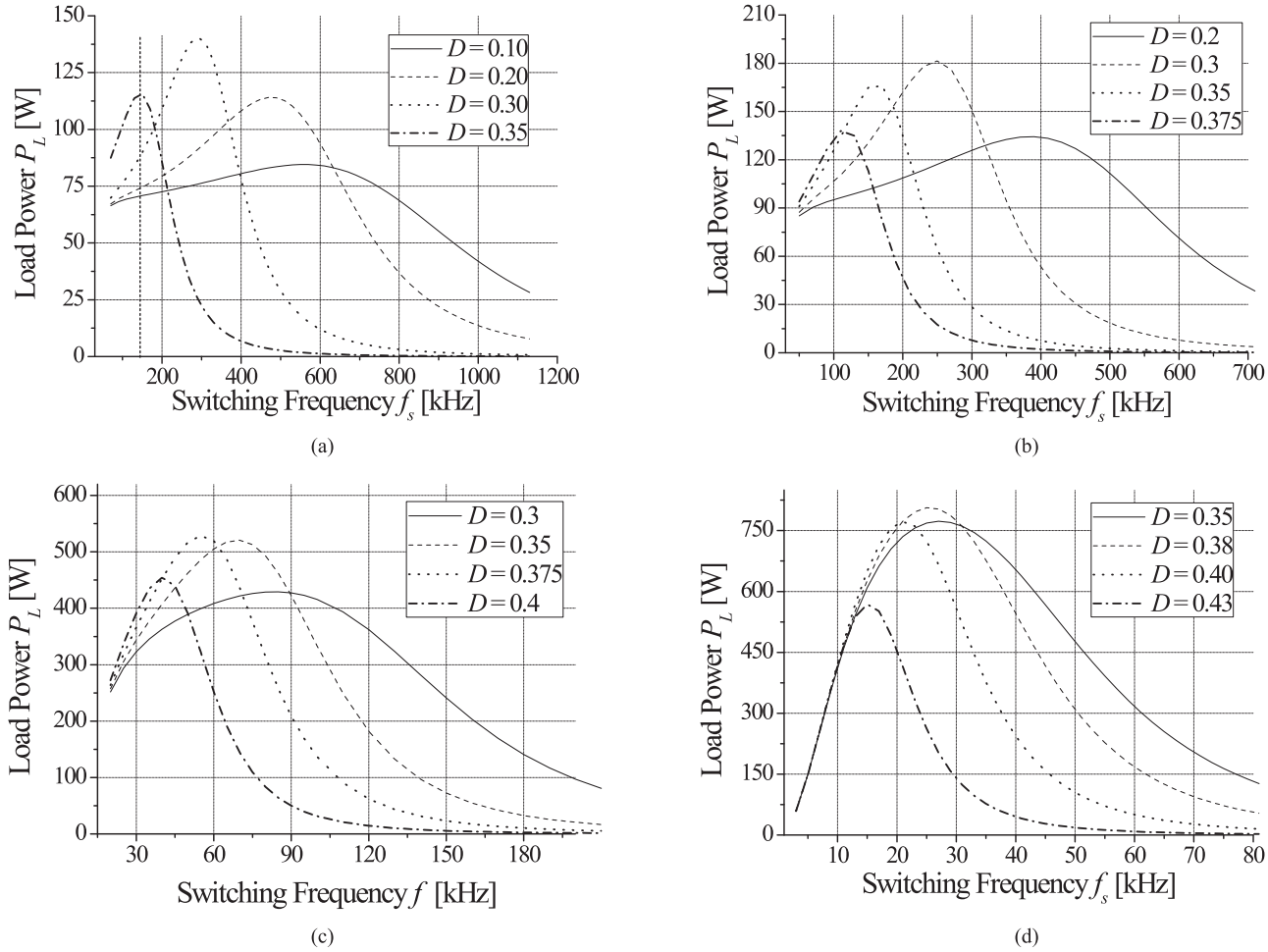

Fig. 13. Calculation results of P_L w.r.t. f_s for various duty D. (a) $d = d_{\max}$. (b) $d = d_2$. (c) $d = d_1$. (d) $d = d_{min}$.

is surely guaranteed. Then, i_c is simply determined as follows:

$$i_c(t) = i_2(t) = -\frac{V_E}{\omega_s L_e}\left(\cos\omega_s t - \cos\omega_s t_1\right) + i_2(t_1) \;\text{ for }\; t_1 < t < t_2. \tag{17}$$

This mode ends when S_1, whose duty cycle is arbitrarily controlled to regulate the load power, is turned OFF.

Mode 3 [t_2, t_3]: At t_2, the switch S_1 is just turned OFF, as shown in Fig. 15(c). Then, v_c is determined, where i_2 is assumed to be constant for a short time period of this mode as follows:

$$v_c(t) \cong \frac{1}{\omega_v C_p}\left(i_2(t_2) - \frac{V_E}{\omega_s L_e}\cos\omega_s t_2\right) \times \sin\omega_v(t - t_2) \;\text{ for }\; t_2 < t < t_3. \tag{18}$$

During this mode, a rising edge of v_{d1} is detected by MCU, as shown in Fig. 3. In this way, the gate signal for negative polarity operation of v_{gs2} will be turned on after the delay time t_d, which can be arbitrarily chosen in the MCU, considering the switching frequency, e.g., $t_d = 1.0\,\mu$s for $f_s = 140$ kHz throughout this paper.

This mode ends when v_c reaches V_L, and the time interval t_{32} can be straightforwardly determined from (18) as follows:

$$t_{32} \cong \frac{1}{\omega_v}\sin^{-1}\left(\frac{\omega_v\omega_s L_e C_p V_L}{\omega_s L_e i_2(t_2) - V_E\cos\omega_s t_2}\right). \tag{19}$$

Mode 4 [t_3, t_4]: At t_3, the diode D_1 and the body-diode of the switch S_2 are turned ON as a result of $v_c(t_3) = V_L$. Then, i_2 can be determined as follows:

$$i_2(t) = \frac{V_E}{\omega_s L_e}\left(\cos\omega_s t_3 - \cos\omega_s t\right) - \frac{V_L}{L_e}(t - t_3) + i_2(t_3) \text{ for } t_3 < t < t_4 \tag{20}$$

During this mode, v_{gs2} is applied to S_2, and margin time $t_m\ (> 0)$ is enough to achieve the ZVS operation of S_2 until the next polarity transition point, as shown in Fig. 15(d). This mode ends when i_2 in (20) becomes zero.

As shown in Fig. 3, load power P_L can be sensed by load voltage and current sensing circuits, and calculated by the MCU for load power regulation. Thus, the feedback of load power PL, f can be obtained and compared to the reference load power PL, r, corresponding to 100 W in this paper. Through this negative feedback control loop by digital controller, an appropriate

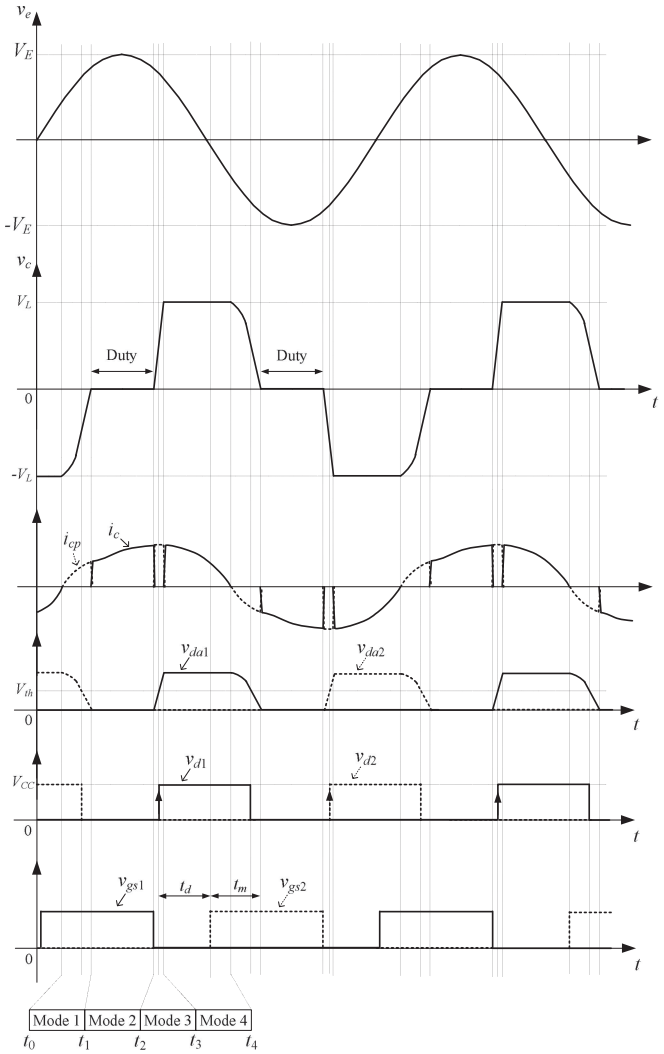

Fig. 14. Waveform diagrams of the proposed IPT.

switching duty cycle d for S1 and S2 is finally determined by the PI control routine by MCU coding for load power regulation against distance variations. Those contents are omitted due to its simple coding tasks in this paper.

V. Experimental Verifications

The design results for the baseline of 100 W IPT will be experimentally verified in this section. In this application, if the coil distance is fixed after installation, it is hardly possible to move Tx or Rx coil due to its large and heavy structures of the proposed IPT. Even though utility line voltage V_s changes, the PFC of SMPS in Fig. 3 shall control the regulated V_{dc}, which corresponds to the input voltage of the proposed IPT. Due to such reasons, dynamic regulation performances by distance d and utility line voltage V_s variations are out of scope in this paper.

A. Fabrication and Parameters Selection

The analysis and design considerations of the proposed IPT are verified by an experimental kit of 100 W load power delivery at the wide-range distance variations of 20 cm $\leq d \leq$ 70 cm. As shown in Fig. 16(a), the fabricated size of the Tx and Rx

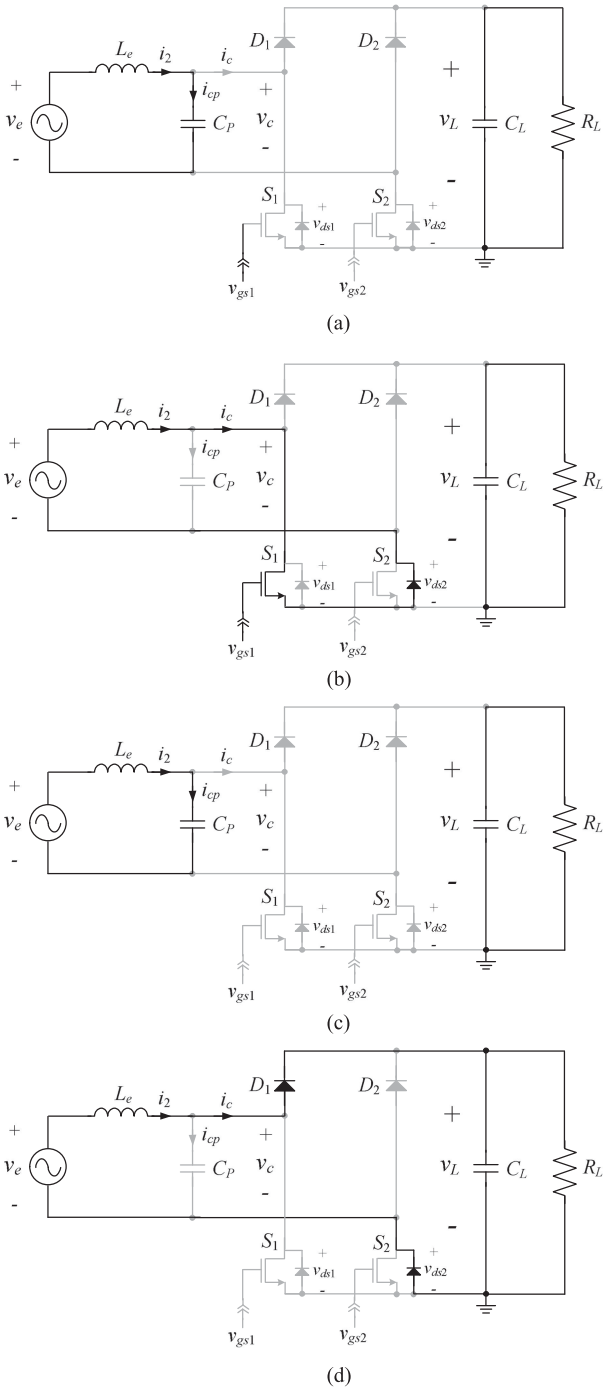

Fig. 15. Operating modes of the proposed IPT. (a) Mode 1. (b) Mode 2. (c) Mode 3. (d) Mode 4.

coils are 100 cm × 5.0 cm × 5.0 cm and 100 cm × 2.5 cm × 5.0 cm, respectively, with an optimized stepped core structure, considering the characteristics of the used core, total weight, and length in this paper [14]–[15]. An aluminum plate, whose length, width, and thickness are 150 cm, 15 cm, and 2 mm, respectively, is adopted as the Tx reflector, which blocks the magnetic flux behind the Tx reflector for human safety and reflects the magnetic flux generated from the Tx coil to Rx coil [23]. The number of turns for Tx and Rx coils N_1 and N_2 are 40 and 70, respectively, and litz wire having 3.0 mm

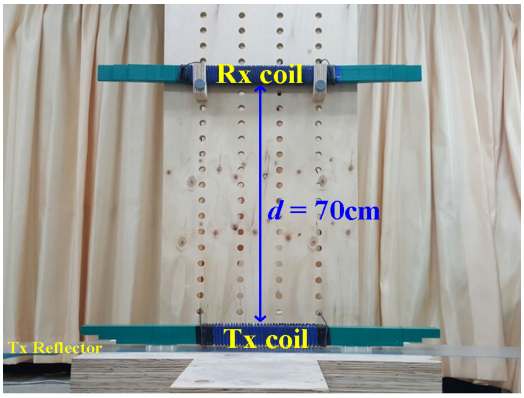

(a)

(b)

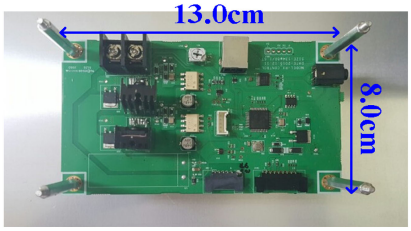

(c)

Fig. 16. Fabricated prototype of the proposed IPT for 100 W load power delivery. (a) Fabricated Tx and Rx coils. (b) Asymmetric half-bridge inverter. (c) Rectifier and control circuit for the variable switched capacitance.

TABLE II
PARAMETER SELECTIONS OF THE PROPOSED IPT

Parameters	Values	Parameters	Values
r_1	8.0 Ω	C_3	0.1 μF
r_2	18.0 Ω	C_4	0.1 μF
R_3	620 kΩ	C_L	5.0 μF
R_4	10 kΩ	V_{th}	3.3 V
R_5	750 kΩ	MCU	STM32F105RCT6
R_6	10 kΩ	Comparator	TLV3502
R_7	0.2 Ω	GD_1, GD_2	TLP250
R_8	3.9 kΩ	S_1, S_2	STD10NM60N
R_9	200 kΩ	$D_1 \sim D_2$	QD606S
R_{10}	300 kΩ	n_1	40
C_1	1.57 nF	n_2	70
C_2	570 pF		

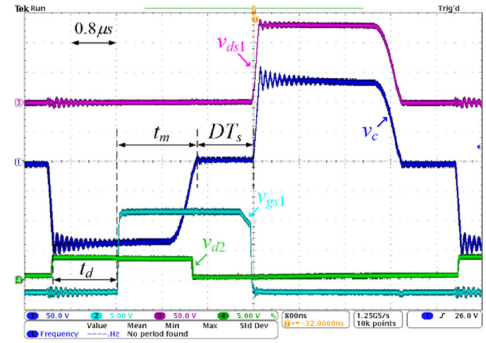

(a)

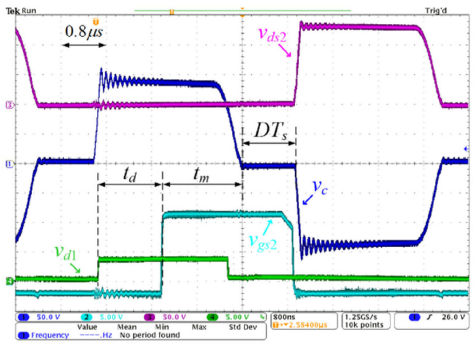

(b)

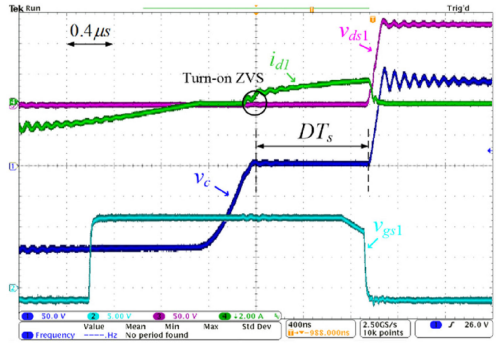

(c)

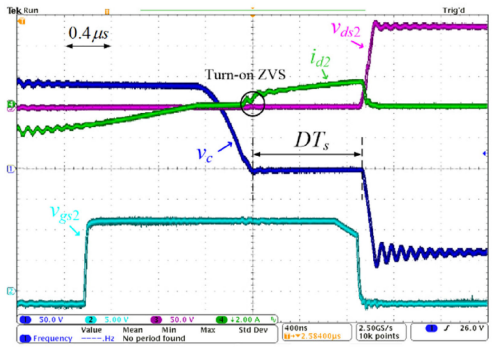

(d)

Fig. 17. Experimental waveforms of the proposed control circuit for ZVS operations of S_1 and S_2 at $d = d_{\max}$ for $P_L = 100$ W. (a) v_c, v_{gs1}, v_{ds1}, and v_{d2}. (b) v_c, v_{gs2}, v_{ds2}, and v_{d1}. (c) v_c, v_{gs1}, v_{ds1}, and i_{ds1}. (d) v_c, v_{gs2}, v_{ds2}, and i_{ds2}.

diameter of thickness was adopted for Tx and Rx windings. The measured internal resistances of the Tx and Rx coils r_1 and r_2 in Fig. 3 were 8.0 Ω and 18.0 Ω, respectively, and the series resonant capacitors C_1 and C_2 were selected as 1.57 nF and 570 pF to fully resonate with L_1 and L_2, respectively. The sensing resistors R_3 and R_4 are selected as 62.0 $k\Omega$ and 1.0 $k\Omega$, considering maximum load voltage level of 300 V to compare $V_{\rm th}$ in Fig. 14, which is generated from the MCU for threshold voltage: $V_{\rm th} = 3.3$ V. $R_5 \sim R_{10}$ with an op-amp is adopted for simply dividing load voltage and sensing load current [38]. A high-frequency operation film capacitor having a capacitance of 5 μF was selected for C_L and the small size of external dc–dc converters, which were connected to the load in parallel, were used to provide V_{CC}, V_{EE} with gate drivers, a comparator, an

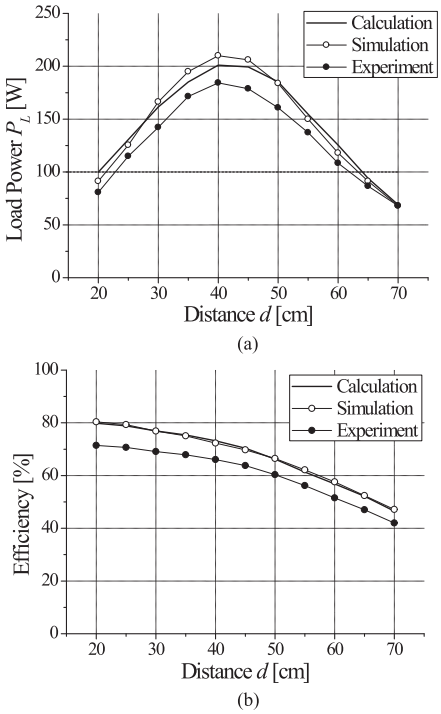

Fig. 18. Experimental results of P_L and η when d changes without the variable switched capacitance, compared with the calculation and simulation results. (a) P_L, (b) η

op-amp, and the MCU. All the parameter values are summarized in Table II based on the design principles.

B. ZVS Operation of the Variable Switched Capacitance Circuit

As identified from Figs. 14 and 15, the operations of the proposed control circuit were experimentally verified for ZVS operations of S_1 and S_2, as shown in Fig. 17. The rising edge of v_{d2} or v_{d1} is detected by the MCU, and gate signal v_{gs1} or v_{gs2} is applied after t_d, as shown in Fig. 17(a) and (b); t_m was measured as 1.44 μs when $t_d = 1.0\,\mu$s for both positive and negative polarities, whose value is still enough to achieve ZVS operations of S_1 and S_2. As a result, the turn-on ZVS operations of S_1 and S_2 were successfully achieved, as shown in Fig. 17(c) and (d), where the turn-OFF ZVS operation will be guaranteed if slow increases of v_{ds1} and v_{ds2} are achieved by the reasonable or large C_p case, as identified from Fig. 4(b) and (c).

C. Load Power Regulation

As identified from Fig. 10 for the proposed design procedure, the characteristics of the load power and power efficiency of the proposed IPT when d changes from $d_{\max}$ to $d_{\min}$ without the variable switched capacitance were verified by simulations and experiments, as shown in Fig. 18. The experimental results showed good agreements with the calculation and simulation results, where a PSIM simulation was performed for the circuit of Fig. 3 without a control circuit. The major discrepancy between the calculation and simulation results is the constant value of $\alpha\,(= 0.75)$ under wide-range distance variation for calculation results from (2)–(7). From Fig. 18, it was experimentally found that $d_{\max} = 70$ cm, $d_2 = 62$ cm, $d_1 = 40$ cm, and $d_{\min} = 23$ cm, and the load power was completely regulated to 100 W by the variable switched capacitance under a wide-range of distance variation $d_v = 47$ cm.

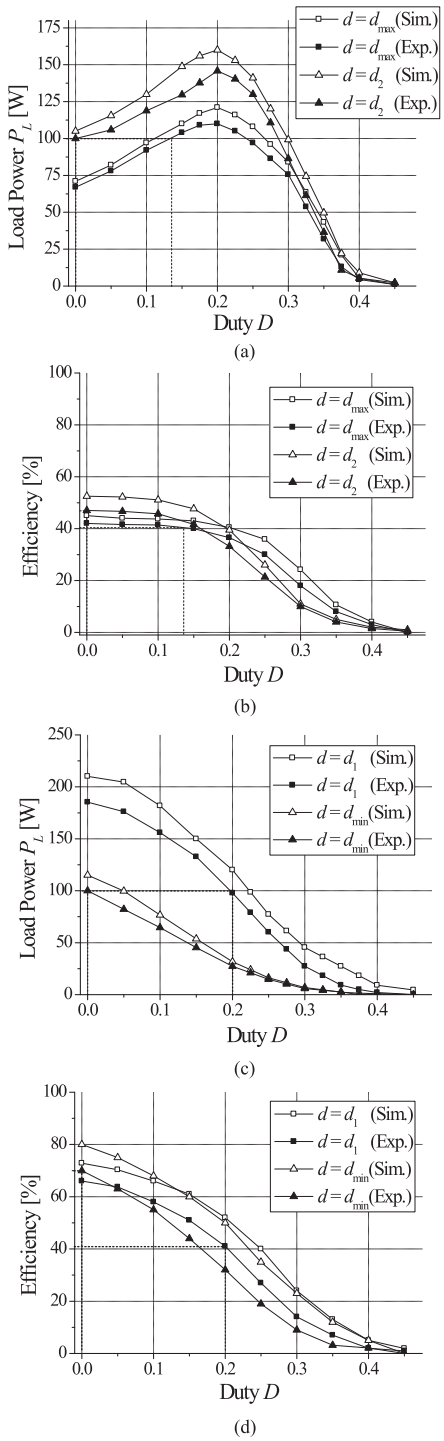

Fig. 19. Experimental results of P_L w.r.t. D for various d. (a) P_L for $d_{\max}$ and d_2, (b) η for $d = d_{\max}$ and d_2, (c) P_L for $d = d_1$ and $d = d_{\min}$, (d) η for $d = d_1$ and $d_{\min}$.

The major behaviors of the variable switched capacitance were verified by simulations and experiments, as shown in Fig. 19. The discrepancies between simulation and experiment results in Figs. 18 and 19 are due to conduction losses of

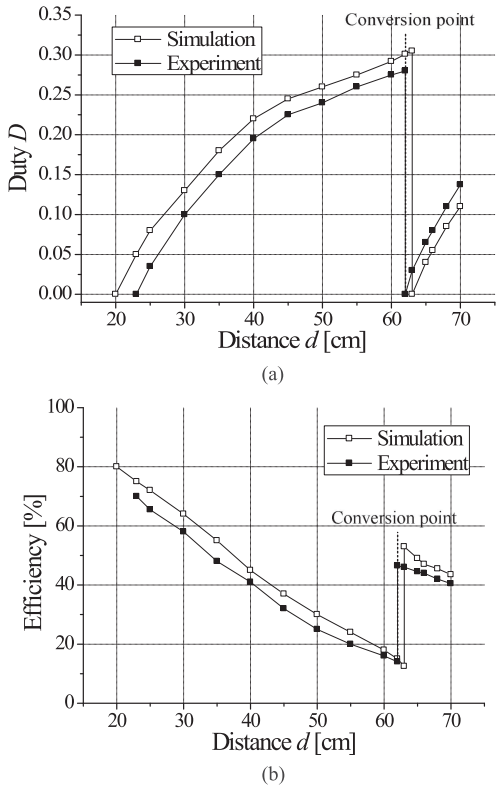

Fig. 20. Experimental results of D and η for the distance variation, satisfying $P_L = 100$ W by D. (a) D, (b) η.

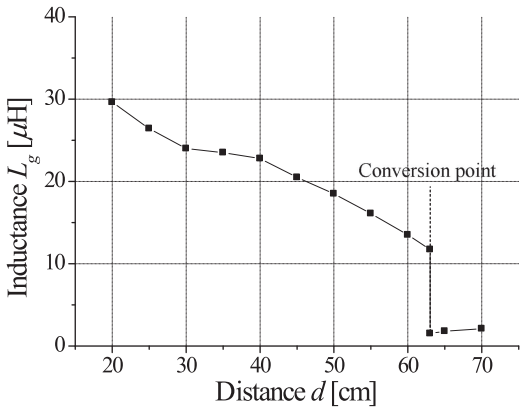

Fig. 21. Inductance L_g variation when load power is regulated by the variable switched capacitance, satisfying $P_L = 100$ W for ZVS operations of M_1 and M_2.

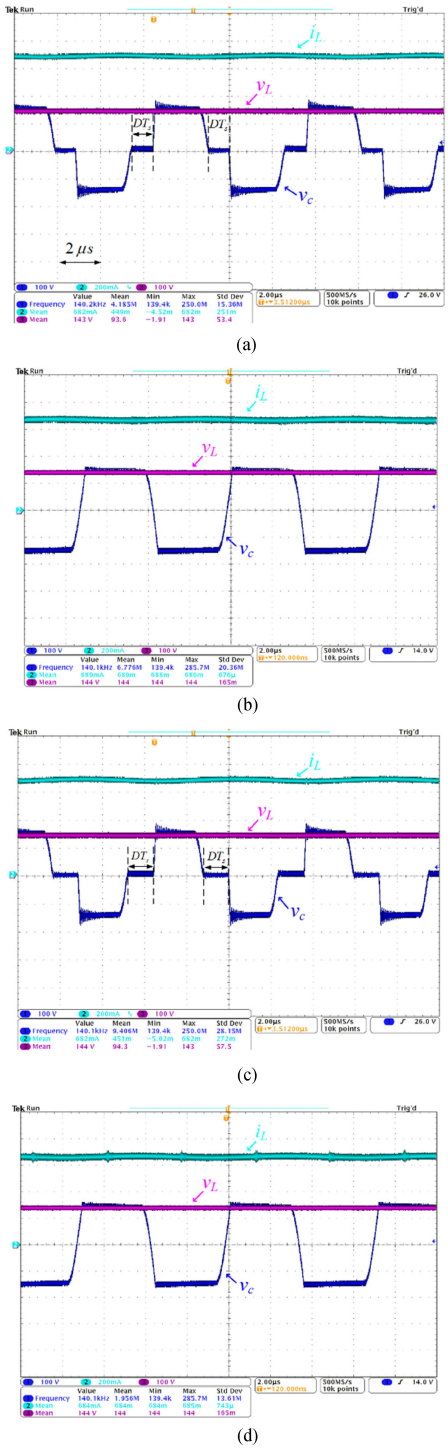

Fig. 22. Experimental waveforms of v_c, v_L, and i_L for various distances, satisfying $P_L = 100$ W. (a) $d = d_{\max}$, (b) $d = d_{d2}$, (c) $d = d_{d1}$, (d) $d = d_{\min}$.

internal resistance of L_a, the half-bridge inverter in Tx circuit, and a diode rectifier in Rx circuit, which are not considered in calculation results and simulation verifications. The measured values do not perfectly match the calculation results in Fig. 12, e.g., the peak value of the P_L at $d = d_{\max}$ was measured as $D = 0.2$, whereas the calculation value was $D = 0.35$. Nevertheless, it is clear that the tendency and characteristics of the proposed IPTS are the same, and the performance of the proposed IPT works perfectly. The major reason for this discrepancy is the nonlinearity of v_c,, i.e., the calculated values of the equivalent capacitance determined by D in (1) did not match well with the simulation and experiment due to a small value of C_p ($= 1$ nF) in this paper, as identified from Section II. Therefore, it is not possible to analytically find the exact value of the equivalent capacitance of C_v determined by D for this nonlinearity case, considering the conversion ratio of α.

The optimum duty, satisfying $P_L = 100$ W under distance variation, can be found from Figs. 18 and 19, as shown in Fig. 20, where conversion point exists. It is because two duty points,

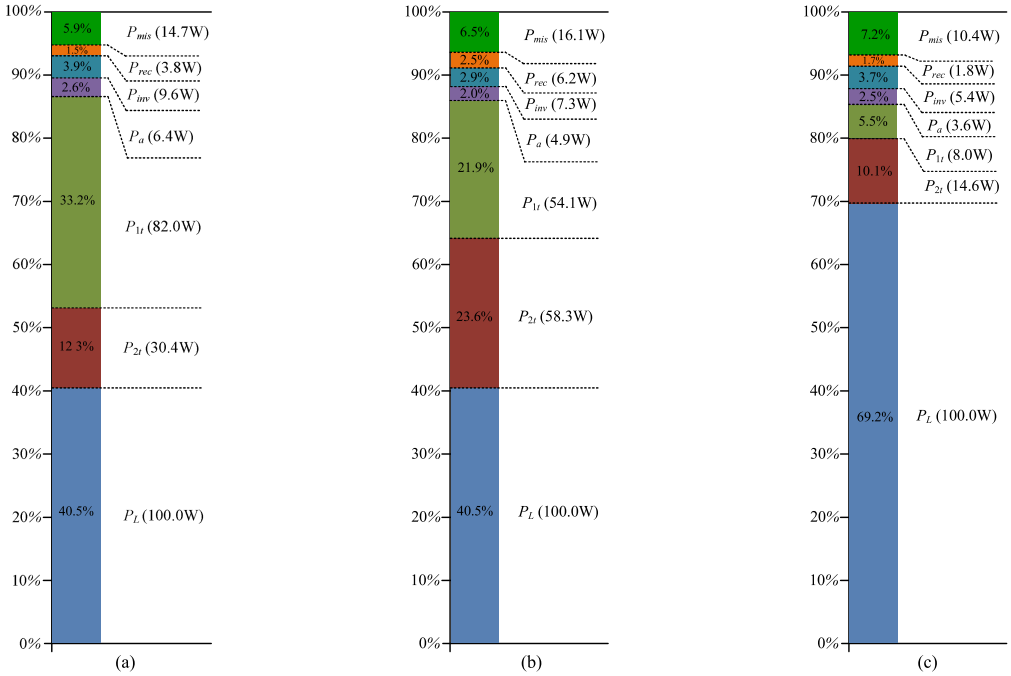

Fig. 23. Power loss analysis of the proposed IPTS. (a) $d = d_{\max}$, (b) $d = d_{d1}$, (c) $d = d_{\min}$.

satisfying $P_L = 100$ W, exist below conversion point range, which corresponds to $d_2 \le d \le d_{\max}$ (62 cm $\le d \le$ 70 cm), as shown in Fig. 19(a). Even though both duty points are available for $P_L = 100$ W, a lower duty is recommended due to its higher efficiency for $d_2 \le d \le d_{\max}$, as shown in Fig. 19(b). Concerning control method of adopting a lower duty among two duty points for $d_2 \le d \le d_{\max}$, switching duty cycle D starts to be increase from zero until $P_L = 100$ W at the beginning of the control operation. If $P_L = 100$ W, D will stop to increase, which corresponds to a lower duty operation, implemented by MCU in Fig. 3. Therefore, a lower duty is automatically chosen as an optimum duty point for high efficiency. On the other hands, above conversion point range, which corresponds to $d_{\min} \le d < d_2$ (23 cm $\le d <$ 62 cm), only one duty point exists for $P_L = 100$ W in Fig. 19(c). The ZVS operations of M_1 and M_2 were experimentally verified, as shown in Fig. 21, where L_g was calculated from (9) based on the distance d and switching duty cycle D. In Fig. 21, L_g is always lower than L_a ($= 70\,\mu$H), which satisfies (11) for ZVS conditions of M_1 and M_2. As shown in Fig. 22, which shows the regulated v_L, i_L, and v_c, the load voltage and current were well regulated to constant values, which corresponds to 100 W of nominal load power $P_{L,\mathrm{nom}}$. As a result, 40.5%, 46.1%, 40.5%, and 69.2% were achieved for $d = d_{\max}$, d_2, d_1, and $d_{\min}$, respectively, for $P_L = 100$ W with 47 cm of very wide-range distance variations.

Although it is not possible to measure all the detail power losses, the power loss analysis of the proposed IPT for three cases is presented, as shown in Fig. 23, where parameter remarks are summarized in Table III. All power losses can be calculated or measured except for the miscellaneous loss, which is the remaining discrepancy that cannot be explained. P_{1t} and P_{2t} can be found by measuring I_1, r_1, I_2, and r_2; however, each component of power loss in P_{1t} and P_{2t} cannot be exactly separated by calculation or experiment, i.e., P_{1e}. Hysteresis losses P_{1h} and P_{2h}, which are the major source of P_{1t} and P_{2t} in Fig. 23, were roughly occupied by 30–40% of P_{1t} and P_{2t} by Steinmetz equation calculations [14]. Dominant losses are found to be P_{1t} and P_{2t}, whose loss portions become decrease when the distance decreases due to decrement of Tx and Rx coil currents of I_1 and I_2. Especially, P_{2t} at $d = d_1$ becomes relatively larger compared to the other distance cases, which mainly comes from large switching duty cycle of proposed variable switched capacitance, as identified from Fig. 20(a). Therefore, a better ferrite core will be required to be developed in order to improve the power efficiency for the long distance IPT.

TABLE III
NOMENCLATURES FOR POWER LOSS ANALYSIS

Parameters	Remarks	Parameters	Remarks
P_{mis}	Miscellaneous loss	$P_{1\mathrm{h}}$	Hysteresis loss of Tx coil
P_{rec}	Conduction loss in rectifier for Rx coil	$P_{2\mathrm{t}}$	Total loss in Rx coil ($= P_{2\mathrm{c}}+P_{2\mathrm{e}}+P_{2\mathrm{h}}$)
P_{inv}	Conduction loss in inverter for Tx coil	$P_{2\mathrm{c}}$	Copper loss of Rx coil
P_{a}	Conduction loss by L_{a} and C_{a}	$P_{2\mathrm{e}}$	Eddy current loss of Rx coil
$P_{1\mathrm{t}}$	Total loss in Tx coil ($= P_{1\mathrm{c}}+P_{1\mathrm{e}}+P_{1\mathrm{h}}$)	$P_{2\mathrm{h}}$	Hysteresis loss of Rx coil
$P_{1\mathrm{c}}$	Copper loss of Tx coil	P_L	Load power
$P_{1\mathrm{e}}$	Eddy current loss of Tx coil		

VI. Evaluation of the Conversion Ratio by Experiment

It has been proven that the conversion ratio α in (2) is nearly 0.9 in the case of the CCM of the diode rectifier [42]–[46]. However, in the case of the DCM of the diode rectifier, it

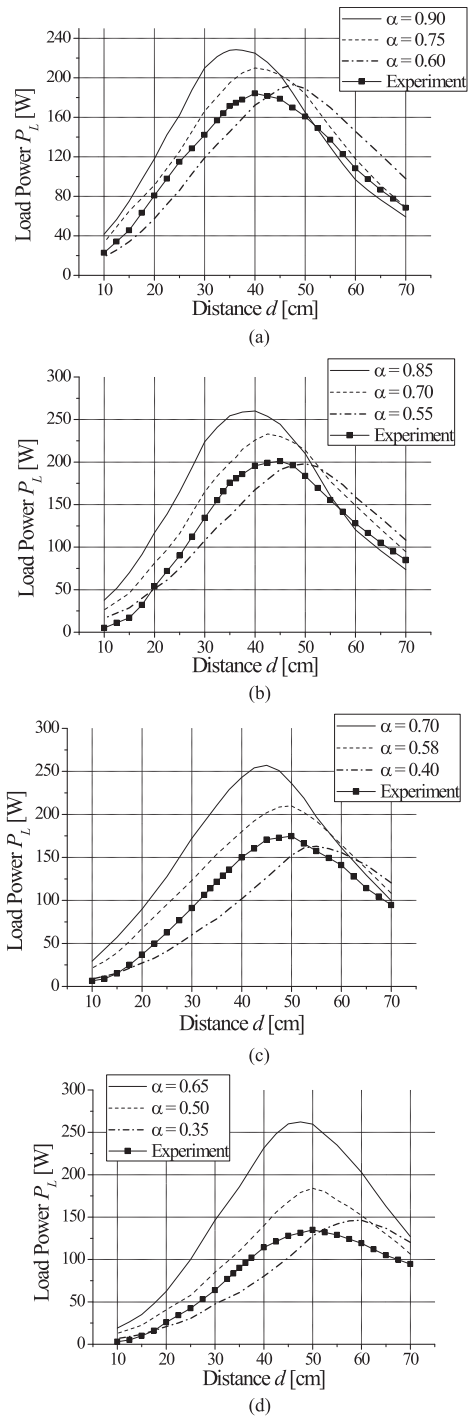

Fig. 24. Comparison of the experimental results with theoretical results by different conversion ratio α for various C_p. (a) $C_p = 1.0$ nF. (b) $C_p = 2.2$ nF. (c) $C_p = 4.4$ nF. (d) $C_p = 6.8$ nF.

is almost impossible to analytically find the exact value of α for different charging times of t_{c1} and t_{c2} in Fig. 4 due to its nonlinearity of v_c [42]–[46]. Note that if an effective turn-ON period of the diode rectifier is reduced by large parallel capacitance C_p, α decreases; hence, α is determined by C_p if other parameters are fixed, and α cannot be arbitrarily chosen for the design procedure. Instead, the optimum values of α for different C_p have been found by comparing the experimental results with the theoretical results of load power from (7), as shown in Fig. 24.

As identified from Fig. 24, the different optimum values of α are found according to C_p where all parameter conditions are identical: $\alpha = 0.75$, 0.70, 0.58, and 0.50 for $C_p =$ 1.0 nF, 2.2 nF, 4.4 nF and 6.8 nF, respectively. It is certain that large C_p requires a small value of α, and this is why α was selected as 0.75 for $C_p = 1\,nF$ throughout this paper.

VII. Conclusion

Dipole-coil-based IPT with the Tx reflector, which regulates the load power successfully under very wide-range distance variation, has been fully verified throughout this paper. The load power of 100 W was completely regulated by the variable switched capacitance, and no bulky passive components such as inductors, transformers, and electrolytic capacitors were used in the Rx circuit, which makes the proposed IPT system simple, compact, and low cost manufacture. By proposed gyrator-based static analysis and secondary control circuit, reliable ZVS conditions of both $M_1\&M_2$ and $S_1\&S_2$ have been successfully realized. As a result, the Tx and Rx coils can be arbitrarily placed within 47 cm of very wide-range distance variation, which is one of the main issues for WPT applications. Therefore, it is expected that the proposed IPT can be applied to not only home appliances, which usually require power consumptions of around 100 W, but also high power applications, e.g., electric vehicles having larger than 1 kW, by virtue of the variable switched capacitance capable of adaptive modulation of LC resonant frequency.

References

[1] A. Kurs *et al.*, "Wireless power transfer via strongly coupled magnetic resonances," *Science*, vol. 317, pp. 83–86, Jul. 2007.
[2] B. H. Choi, E. S. Lee, J. Huh, and C. T. Rim, "Lumped impedance transformers for compact and robust coupled magnetic resonance systems," *IEEE Trans. Power Electron.*, vol. 30, no. 11, pp. 6046–6056, Nov. 2015.
[3] Z. Yan, Y. Li, C. Zhang, and Q. Yang, "Influence factors analysis and improvement method on efficiency of wireless power transfer via coupled magnetic resonance," *IEEE Trans. Magn.*, vol. 50, no. 4, pp. 1–4, Apr. 2014.
[4] B. Wang, W. Yerazunis, and K. Teo, "Wireless power transfer: metamaterials and array of coupled resonators," *Proc. IEEE*, vol. 101, no. 6, pp. 1359–1368, Jun. 2013.
[5] H. Hwang *et al.*, "An analysis of magnetic resonance coupling effects on wireless power transfer by coil inductance and placement," *IEEE Trans. Consum. Electron.*, vol. 60, no. 2, pp. 203–209, May 2014.
[6] A. P. Sample, D. A. Meyer, and J. R. Smith, "Analysis, experimental results, and range adaption of magnetically coupled resonators for wireless power transfer," *IEEE Trans. Ind. Electron.*, vol. 58, no. 2, pp. 544–554, Feb. 2011.
[7] J. Kim *et al.*, "Coil design and shielding methods for a magnetic resonant wireless power transfer system," *Proc. IEEE*, vol. 101, no. 6, pp. 1332–1342, Jun. 2013.
[8] E. Y. Chow *et al.*, "Wireless powering and the study of RF propagation through ocular tissue for development of implantable sensors," *IEEE Trans. Antennas Propag.*, vol. 59, no. 6, pp. 2379–2387, Jun. 2011.
[9] M. W. Baker *et al.*, "Feedback analysis and design of RF power links for low-power bionic systems," *IEEE Trans. Biomed. Circuits Syst.*, vol. 1, no. 1, pp. 28–38, Mar. 2007.
[10] M. Han *et al.*, "High efficient rectenna using a harmonic rejection low pass filter for RF based wireless power transmission," in *Proc. IEEE Int. Symp. Wireless Commun. Syst.*, Aug. 2014, pp. 423–426.

[11] K. Sankaragomathi *et al.*, "A 27μW subcutaneous wireless biosensing platform with optical power and data transfer," in *Proc. IEEE Custom Integr. Circuits Conf.*, Sep. 2014, pp. 1–4.

[12] N. Wang *et al.*, "One-to-multipoint laser remote power supply system for wireless sensor networks," *IEEE Sens. J.*, vol. 12, no. 2, pp. 389–396, Feb. 2012.

[13] J. Fakidis *et al.*, "Indoor optical wireless power transfer to small cells at nighttime," *IEEE J. Lightw. Technol.*, vol. 34, no. 13, pp. 3236–3258, Apr. 2016.

[14] C. Park, S. Lee, G. H. Cho, and C. T. Rim, "Innovative 5m-off-distance inductive power transfer systems with optimum shaped dipole coils," *IEEE Trans. Power Electron.*, vol. 30, no. 2, pp. 817–827, Feb. 2015.

[15] B. H. Choi, V. X. Thai, E. S. Lee, J. H. Kim, and C. T. Rim, "Dipole-coil-based wide-range inductive power transfer systems for wireless sensors," *IEEE Trans. Ind. Electron.*, vol. 63, no. 5, pp. 3158–3167, Jan. 2016.

[16] R. Hui, W. Zhong, and C. Lee, "A critical review of recent progress in mid-range wireless power transfer," *IEEE Trans. Power Electron.*, vol. 29, no. 9, pp. 4500–4511, Sep. 2014.

[17] Z. N. Low, R. A. Chinga, R. Tseng, and J. Lin, "Design and test of a high-power high-efficiency loosely coupled planar wireless power transfer system," *IEEE Trans. Ind. Electron.*, vol. 56, no. 5, pp. 1801–1812, May 2009.

[18] M. Budhia *et al.*, "Development of a single-sided flux magnetic coupler for electric vehicle IPT charging systems," *IEEE Trans. Ind. Electron.*, vol. 60, no. 1, pp. 318–328, Jan. 2013.

[19] C. K. Lee, W. X. Zhong, and S. Y. R. Hui, "Effects of magnetic coupling of nonadjacent resonators on wireless power transfer domino-resonator systems," *IEEE Trans. Power Electron.*, vol. 27, no. 4, pp. 1905–1916, Apr. 2012.

[20] G. Elliott, S. Raabe, G. Covic, and J. Boys, "Multiphase pickups for large lateral tolerance contactless power-transfer systems," *IEEE Trans. Ind. Electron.*, vol. 57, no. 5, pp. 1590–1598, May 2010.

[21] H. Wu, G. Covic, J. Boys, and D. Robertson, "A series-tuned inductive-power-transfer pickup with a controllable AC-voltage output," *IEEE Trans. Power Electron.*, vol. 26, no. 1, pp. 98–109, Jan. 2011.

[22] N. Keeling, G. Covic, and J. Boys, "A unity-power-factor IPT pickup for high-power applications," *IEEE Trans. Ind. Electron.*, vol. 57, no. 2, pp. 744–751, Feb. 2010.

[23] D. T. Nguyen *et al.*, "Optimal shaped dipole-coil design and experimental verification of inductive power transfer system for home applications," in *Proc. IEEE Appl. Power Electron. Conf. Expo.*, Mar. 2016, pp. 1773–1779.

[24] S. Aldhaher, P. C.-K. Luk, and J. F. Whidborne, "Electronic tuning of misaligned coils in wireless power transfer systems," *IEEE Trans. Power Electron.*, vol. 29, no. 11, pp. 5975–5982, Nov. 2014.

[25] S. Aldhaher *et al.*, "Wireless power transfer using class E inverter with saturable DC-feed inductor," *IEEE Trans. Ind. Appl.*, vol. 50, no. 4, pp. 2710–2718, Jul./Aug. 2014.

[26] H. Li *et al.*, "A maximum efficiency point tracking control scheme for wireless power transfer systems using magnetic resonant coupling," *IEEE Trans. Power Electron.*, vol. 30, no. 7, pp. 3998–4008, Jul. 2015.

[27] W. X. Zhong and S. Y. R. Hui, "Maximum energy efficiency tracking for wireless power transfer systems," *IEEE Trans. Power Electron.*, vol. 30, no. 7, pp. 4025–4034, Jul. 2015.

[28] J. M. Miller, O. C. Onar, and M. Chinthavali, "Primary-side power flow control of wireless power transfer for electric vehicle charging," *IEEE J. Emerg. Sel. Topics Power Electron.*, vol. 3, no. 1, pp. 147–162, Mar. 2015.

[29] N. Y. Kim, K. Y. Kim, J. Choi, and C.-W. Kim, "Adaptive frequency with power-level tracking system for efficient magnetic resonance wireless power transfer," *IEEE Electron. Lett.*, vol. 48, no. 8, pp. 452–454, Apr. 2012.

[30] X. Dai *et al.*, "An accurate frequency tracking method based on short current detection for inductive power transfer system," *IEEE Trans. Ind. Electron.*, vol. 61, no. 2, pp. 776–783, Feb. 2014.

[31] S.-J. Huang *et al.*, "Method of feedback detection for loosely coupled inductive power transfer system with frequency-tracking mechanism," in *Proc. IEEE 10th Int. Conf. Power Electron. Drive Syst.*, Apr. 2013, pp. 784–787.

[32] A. W. Green and J. T. Boys, "10 kHz inductively coupled power transfer-concept and control," in *Proc. IEEE 5th Power Electron. Variable-Speed Drives*, Oct. 1994, pp. 694–699.

[33] P. Si *et al.*, "A frequency control method for regulating wireless power to implantable devices," *IEEE Trans. Biomed. Circuits Syst.*, vol. 2, no. 1, pp. 22–29, Mar. 2008.

[34] G. A. Covic *et al.*, "Self tuning pick-ups for inductive power transfer," in *Proc. IEEE Power Electron. Spec. Conf.*, Jun. 2008, pp. 3489–3494.

[35] H. H. Wu *et al.*, "A practical 1.2kW inductive power transfer lighting system using AC processing controllers," in *Proc. IEEE 6th Conf. Ind. Electron. Appl.*, Jun. 2011, pp. 345–350.

[36] U. W. Hsu *et al.*, "Implicit adaptive controller for wireless power pickups," in *Proc. IEEE 6th Conf. Ind. Electron. Appl.*, Jun. 2011, pp. 514–519.

[37] P. Si *et al.*, "Switching frequency analysis of dynamically detuned ICPT power pick-ups," in *Proc. IEEE Int. Conf. Power Syst. Technol.*, Oct. 2006, pp. 1–8.

[38] E. S. Lee *et al.*, "Versatile LED drivers for various electronic ballasts by variable switched capacitor," *IEEE Trans. Power Electron.*, vol. 31, no. 2, pp. 1489–1502, Feb. 2016.

[39] K. Colak *et al.*, "A novel phase-shift control of semibridgeless active rectifier for wireless power transfer," *IEEE Trans. Power Electron.*, vol. 30, no. 11, pp. 6288–6297, Nov. 2015.

[40] K. Colak *et al.*, "A novel LLC resonant converter with semi bridgeless active rectifier," in *Proc. IEEE Transp. Electrification Conf. Expo*, Jun. 2014, pp. 15–18.

[41] Erdem Asa *et al.*, "Analysis of a CLL resonant converter with semi-bridgeless active rectifier and hybrid control," *IEEE Trans. Ind. Electron.*, vol. 62, no. 11, pp. 6877–6886, Nov. 2015.

[42] S. Lee, B. Choi, and C. T. Rim, "Dynamics characterization of the inductive power transfer system for online electric vehicles by Laplace phasor transform," *IEEE Trans. on Power Electron.*, vol. 28, no. 12, pp. 5902–5909, Dec. 2013.

[43] C. T. Rim and G. H. Cho, "Phasor transformation and its application to the DC/AC analyses of frequency/phase controlled series resonant converters (SRC)," *IEEE Trans. Power Electron.*, vol. 5, no. 2, pp. 201–211, Apr. 1990.

[44] C. T. Rim, D. Y. Hu, and G. H. Cho, "Transformers as equivalent circuits for switches: General proofs and D-Q transformation-based analysis," *IEEE Trans. Ind. Appl.*, vol. 26, no. 4, pp. 777–785, Jul./Aug. 1990.

[45] C. T. Rim, "Unified general phasor transformation for AC converters," *IEEE Trans. Power Electron.*, vol. 26, no. 9, pp. 2465–2475, Sep. 2011.

[46] E. S. Lee *et al.*, "Temperature-robust LC^3 passive LED drivers with low THD, high efficiency and PF, and long life," *IEEE J. Emerg. Sel. Topics Power Electron.*, vol. 3, no. 3, pp. 829–840, Sep. 2015.

[47] ENERGY STAR, Program Requirements For Solid State Lighting Luminaires, *Eligibility Criteria – Version 1.1, ENERGY STAR*, Washington, DC, USA, 2016.

[48] *Limits for Harmonic Current Emissions (Equipment Input Current ≤ 16A per Phase)*, IEC 61000-3-2 class C standard, 2016.

[49] Y. H. Sohn *et al.*, "Gyrator-based analysis of resonant circuits in inductive power transfer systems," *IEEE Trans. Power Electron.*, vol. 31, no. 10, pp. 6824–6843, Oct. 2016.

[50] Y. H. Sohn *et al.*, "General unified analyses of two-capacitor inductive power transfer systems: Equivalence of current-source SS and SP compensations," *IEEE Trans. Power Electron.*, vol. 30, no. 11, pp. 6030–6045, Nov. 2015.

Eun S. Lee (S'13) was born in South Korea in 1986. He received the B.S. degree in electrical engineering from Inha University, Incheon, South Korea, in 2012, and the M.S. degree in nuclear and quantum engineering from the Korea Advanced Institute of Science and Technology (KAIST), Daejeon, South Korea, in 2014. Since 2014, he is currently working toward the Ph.D. degree at KAIST, Daejeon, South Korea.

His current research interests are in the field of power converters, LED drivers, and wireless power transfer systems.

Byeong G. Choi (S'15) was born in South Korea in 1990. He received the B.S. degree in mechanical engineering from Pusan National University, Busan, South Korea, in 2015. He is currently working toward the Integrated Master's Ph.D. degree in nuclear and quantum engineering at Korea Advanced Institute of Science and Technology, Daejeon, South Korea, in 2016.

His current research interests are in the field of power converters and wireless power transfer systems.

Jin S. Choi (S'16) was born in South Korea in 1991. He received the B.S. and M.S. degrees in electrical engineering from the Korea Advanced Institute of Science and Technology (KAIST), Daejeon, South Korea, in 2014, and 2016, respectively. Since 2016, he has been working toward the Ph.D. degree at KAIST, Daejeon, South Korea.

His current research interests are in the field of wireless power transfer systems.

Duy T. Nguyen (S'14–M'16) was born in Vietnam, in 1987. He received the B.S. degree in electrical engineering from the Ho Chi Minh City University of Technology, Vietnam, in 2010. He received the M.S. degree in nuclear and quantum engineering from the Korea Advanced Institute of Science and Technology, Daejeon, South Korea, in 2015.

He is now a Senior Electronic Researcher at MKS Instruments Inc., Daejeon, South Korea. His main responsibilities are to design RF generators, e.g., 60 MHz, Elite+370kHz/450kHz, electronic variable capacitors (eVC) for matching network 13.56 MHz, and power system in RFGs.

Chun T. Rim (M'90–SM'11) was born in South Korea in 1963. He received the B.S. degree with Honor in electrical engineering from the Kumoh Institute of Technology (KIT), South Korea, in 1985, and the M.S. and Ph.D. degrees in electrical engineering from the Korea Advanced Institute of Technology (KAIST), South Korea, in 1987 and 1990, respectively.

Since 2016, he has been a Full Professor of Graduate Program of Energy Technology at GIST. He has been developing various wireless power technologies and leading Mobile Power Electronics Lab (Tesla Lab) at GIST. From 2007 to 2016, he was an Associate Professor of nuclear and quantum engineering at KAIST, where he has developed various power electronics technologies including inductive power transfer for On-Line Electrical Vehicles (OLEV) and led the Nuclear Power Electronics and Robots Lab (PEARL) at KAIST. From 1990 to 1995, he was a Military Officer at the Ministry of National Defense in South Korea. From 1995 to 2003, he was a Senior Researcher at the Agency for Defense Development, Daejeon, and from 1997 to 1999, he was with Astrium in Portsmouth, U.K. From 2003 to 2007, he was the Senior Director at the Presidential Office, Seoul, South Korea. He was involved in developing Korea's first airborne and spaceborne synthetic aperture radars. His research areas include wireless electric vehicles, wireless power systems for robots, drones, mobiles, wearables and IoT, and general unified modeling of power electronics. He has authored or coauthored 167 technical papers, written 16 books including Phasor Power Electronics published in 2016, and holds 155 patents (awarded and pending).

Dr. Rim is currently an Associate Editor of IEEE TRANSACTIONS ON POWER ELECTRONICS and the *Journal of Emerging and Selected Topics in Power Electronics* (J-ESTPE), a Guest Editor of the *Special Issue on Wireless Power Transfer* of the IEEE TRANSACTIONS ON POWER ELECTRONICS, IEEE TRANSACTIONS ON INDUSTRIAL ELECTRONICS, and *J-ESTPE*, a General Chair of the 2014 IEEE VTC-Workshop on Wireless power (WoW) and 2015 IEEE WoW, and general Co-Chair of 2016 IEEE WoW and 2017 IEEE WoW. He received numerous awards including the Best Paper Awards of IEEE POWER ELECTRONICS TRANSACTIONS in 2015 and IEEE JOURNAL OF EMERGING AND SELECTED TOPICS IN POWER ELECTRONICS in 2016 for wireless power, and three prizes by the Korean government. He was the Chair of Wireless Power Committee of KIPE from 2010 to 2015 and the Chair of EV Charger Committee of KIEE since 2011, respectively.